Evidence of a geomagnetic effect on extensive air showers detected with the ARGO-YBJ experiment

B. Bartoli,[1,2] P. Bernardini,[3,4,*] X. J. Bi,[5] I. Bolognino,[6,7] P. Branchini,[8] A. Budano,[8] A. K. Calabrese Melcarne,[3,4] P. Camarri,[9,10] Z. Cao,[5] R. Cardarelli,[10] S. Catalanotti,[1,2] S. Z. Chen,[5] T. L. Chen,[11] Y. Chen,[5] P. Creti,[4] S. W. Cui,[12] B. Z. Dai,[13] A. D'Amone,[3,4] Danzengluobu,[11] I. De Mitri,[3,4] B. D'Ettorre Piazzoli,[1,2] T. Di Girolamo,[1,2] X. H. Ding,[11] G. Di Sciascio,[10] C. F. Feng,[14] Zhaoyang Feng,[5] Zhenyong Feng,[15] Q. B. Gou,[5] Y. Q. Guo,[5] H. H. He,[5] Haibing Hu,[11] Hongbo Hu,[5] Q. Huang,[15] M. Iacovacci,[1,2] R. Iuppa,[9,10] H. Y. Jia,[15] Labaciren,[11] H. J. Li,[11] J. Y. Li,[14] X. X. Li,[5] G. Liguori,[6,7] C. Liu,[5] C. Q. Liu,[13] J. Liu,[13] M. Y. Liu,[11] H. Lu,[5] X. H. Ma,[5] G. Mancarella,[3,4] S. M. Mari,[8,16] G. Marsella,[3,4] D. Martello,[3,4] S. Mastroianni,[2] P. Montini,[8,16] C. C. Ning,[11] M. Panareo,[3,4] B. Panico,[9,10] L. Perrone,[3,4] P. Pistilli,[8,16] F. Ruggieri,[8] P. Salvini,[7] R. Santonico,[9,10] S. N. Sbano,[3,4] P. R. Shen,[5] X. D. Sheng,[5] F. Shi,[5] A. Surdo,[4] Y. H. Tan,[5] P. Vallania,[17,18] S. Vernetto,[17,18] C. Vigorito,[18,19] B. Wang,[5] H. Wang,[5] C. Y. Wu,[5] H. R. Wu,[5] B. Xu,[15] L. Xue,[14] Y. X. Yan,[13] Q. Y. Yang,[13] X. C. Yang,[13] Z. G. Yao,[5] A. F. Yuan,[11] M. Zha,[5] H. M. Zhang,[5] Jilong Zhang,[5] Jianli Zhang,[5] L. Zhang,[13] P. Zhang,[13] X. Y. Zhang,[14] Y. Zhang,[5] Zhaxiciren,[11] Zhaxisangzhu,[11] X. X. Zhou,[15] F. R. Zhu,[15] Q. Q. Zhu,[5] and G. Zizzi[20]

(ARGO-YBJ Collaboration)

[1]*Dipartimento di Fisica dell'Università di Napoli "Federico II,"*
Complesso Universitario di Monte Sant'Angelo, via Cinthia, 80126 Napoli, Italy
[2]*Istituto Nazionale di Fisica Nucleare, Sezione di Napoli, Complesso Universitario di Monte Sant'Angelo, via Cinthia, 80126 Napoli, Italy*
[3]*Dipartimento Matematica e Fisica "Ennio De Giorgi," Università del Salento, via per Arnesano, 73100 Lecce, Italy*
[4]*Istituto Nazionale di Fisica Nucleare, Sezione di Lecce, via per Arnesano, 73100 Lecce, Italy*
[5]*Key Laboratory of Particle Astrophysics, Institute of High Energy Physics, Chinese Academy of Sciences, P.O. Box 918, 100049 Beijing, People's Republic of China*
[6]*Dipartimento di Fisica dell'Università di Pavia, via Bassi 6, 27100 Pavia, Italy*
[7]*Istituto Nazionale di Fisica Nucleare, Sezione di Pavia, via Bassi 6, 27100 Pavia, Italy*
[8]*Istituto Nazionale di Fisica Nucleare, Sezione di Roma Tre, via della Vasca Navale 84, 00146 Roma, Italy*
[9]*Dipartimento di Fisica dell'Università di Roma "Tor Vergata," via della Ricerca Scientifica 1, 00133 Roma, Italy*
[10]*Istituto Nazionale di Fisica Nucleare, Sezione di Roma Tor Vergata, via della Ricerca Scientifica 1, 00133 Roma, Italy*
[11]*Tibet University, 850000 Lhasa, Xizang, People's Republic of China*
[12]*Hebei Normal University, Shijiazhuang 050016, Hebei, People's Republic of China*
[13]*Yunnan University, 2 North Cuihu Road, 650091 Kunming, Yunnan, People's Republic of China*
[14]*Shandong University, 250100 Jinan, Shandong, People's Republic of China*
[15]*Southwest Jiaotong University, 610031 Chengdu, Sichuan, People's Republic of China*
[16]*Dipartimento di Fisica dell'Università "Roma Tre," via della Vasca Navale 84, 00146 Roma, Italy*
[17]*Istituto di Fisica dello Spazio Interplanetario dell'Istituto Nazionale di Astrofisica, corso Fiume 4, 10133 Torino, Italy*
[18]*Istituto Nazionale di Fisica Nucleare, Sezione di Torino, via Pietro Giuria 1, 10125 Torino, Italy*
[19]*Dipartimento di Fisica Generale dell'Università di Torino, via Pietro Giuria 1, 10125 Torino, Italy*
[20]*Istituto Nazionale di Fisica Nucleare - CNAF, Viale Berti-Pichat 6/2, 40127 Bologna, Italy*

The geomagnetic field causes not only the east-west effect on primary cosmic rays but also affects the trajectories of the secondary charged particles in the shower, causing their lateral distribution to be stretched. Thus, both the density of the secondaries near the shower axis and the trigger efficiency of detector arrays decrease. The effect depends on the direction of the showers, thus, introducing a modulation in the measured azimuthal distribution. The azimuthal distribution of the events collected by the ARGO-YBJ detector is deeply investigated for different zenith angles in light of this effect.

---

*Corresponding author.
paolo.bernardini@le.infn.it

I. INTRODUCTION

The path of charged primary cosmic rays (CRs) is deflected by magnetic fields. The galactic magnetic field randomizes the CR arrival directions. The geomagnetic field (GeoMF) prevents low-rigidity CRs from reaching the terrestrial atmosphere and causes the east-west asymmetry (the CR flux from the east is lower than that from the west) [1]. The GeoMF acts also on the charged particles of the extensive air showers (EAS) during their travel in the atmosphere. Cocconi [2] suggested that the lateral displacement induced by the Earth's magnetic field is not negligible with respect to the Coulomb scattering when the shower is young. According to Cocconi's model, the effect could increase for high-altitude measurements. Moreover, if the trigger efficiency of an array is sensitive to the shower lateral extension, the GeoMF can change the acquisition rate as a function of the zenith and azimuth angles. An azimuthal modulation was observed at the Yakutsk array for EAS with energies above 50 PeV [3] and at the ALBORZ Observatory for energies above 100 TeV [4]. The GeoMF effect has been observed in radio experiments [5] and studied to improve the EAS simulation [6], to correct the pointing of Čerenkov telescopes [7], and to discriminate the primary mass [8]. The importance of the GeoMF has been pointed out also in studies on CR large-scale anisotropy [9].

The GeoMF effect in the ARGO-YBJ data has been preliminarily estimated [10] and studied [11]. Here those studies are updated using a very large data sample, and for the first time, the GeoMF lateral stretching is observed at small distances from the shower core.

In Sec. II, the detector features are briefly presented. A simple model of the GeoMF action is sketched in Sec. III, and the results are confirmed by the simulation of CR beams (Sec. IV) assuming different values of the magnetic field. In Sec. V, the modulation of the azimuthal distribution is foreseen as an effect of the GeoMF action. The main data analysis is described in Sec. VI looking for hints of the GeoMF effect in a sample of showers with cores inside the detector. In Sec. VII, showers with external cores are also analyzed, and a check of the pointing accuracy is suggested in Sec. VIII. The conclusions are given in Sec. IX.

II. THE ARGO-YBJ DETECTOR

ARGO-YBJ [12] is an array located at the Yangbajing Cosmic Ray Observatory (Tibet, People's Republic of China), 4300 m above sea level (90°31′50″E, 30°06′38″N). It is mainly devoted to γ-ray astronomy [13] and cosmic ray physics [14]. The detector consists of a 74×78 m² carpet made of a single layer of resistive plate chambers (RPCs) with ~92% of active area surrounded by a partially instrumented (~20%) area up to 100×110 m². The apparatus has a modular structure, the basic data acquisition element being a cluster (5.7×7.6 m²) made up of 12 RPCs (2.8×1.25 m² each). The full experiment is made up of 153 clusters for a total active surface of ~6600 m². The RPCs are operated in streamer mode with a gas mixture (Ar 15%, isobutane 10%, and tetrafluoroethane 75%) suitable for high-altitude operation. Each RPC is read by 80 external strips of 6.75×61.8 cm² (the spatial pixels) that are logically organized in ten independent pads of 55.6×61.8 cm² each, which are individually acquired and represent the time pixels [15]. In addition, in order to extend the dynamical range up to PeV energies, each RPC is equipped with two large pads (1.39×1.23 m² each) to collect the total charge of the particles hitting the detector [16].

ARGO-YBJ operates in two independent acquisition modes: shower and scaler mode [17]. Here the data collected by the digital readout in shower mode have been used. In this mode, an electronic logic has been implemented to build an inclusive trigger based on the time correlation between the pad signals, depending on their relative distances. The showers firing at least N_{trig} pads in the central carpet in a time window of 420 ns generate a trigger. The time of each fired pad within 2 μs around the trigger time and its location are recorded and used to reconstruct the position of the shower core and the direction of the primary particle.

ARGO-YBJ started taking data with its complete layout in November 2007 with the trigger condition $N_{\text{trig}} = 20$. The detector was operated until February 2013 with a duty cycle higher than 86%, a trigger rate of ~3.5 kHz and a dead time of 4%.

Typically, the EAS collected digitally in the shower mode have an energy in the range of 1–200 TeV, well beyond the rigidity cutoff at the YBJ site. Therefore, the effect of the GeoMF on the primary trajectory is negligible.

A. Reference frame

In the ARGO-YBJ reference system, the azimuth angle (ϕ) of the EAS is defined with respect to the detector axes in the counterclockwise direction ($\phi = 0°$ for showers aligned with the x axis and moving towards the positive direction). Thus, the azimuth angle of showers going towards the geographical north is $\phi_N = 71.96° \pm 0.02°$. The quoted error is due to the measurement of the orientation of the detector axes with respect to the geographical reference system.

B. Magnetic features of the site

According to the International Geomagnetic Reference Field model available on the NOAA website [18], the geomagnetic field at YBJ in October 2010 had the following features (module, zenith, and azimuth, respectively) in the ARGO-YBJ reference system:

$$B = 49.7 \; \mu\text{T}, \qquad \theta_B = 46.4°, \qquad \phi_B = 71.89°. \quad (1)$$

The Lorentz force on the EAS charged particles depends on the quantity $B \sin \xi$, where ξ is the angle between $\vec{B}$ and
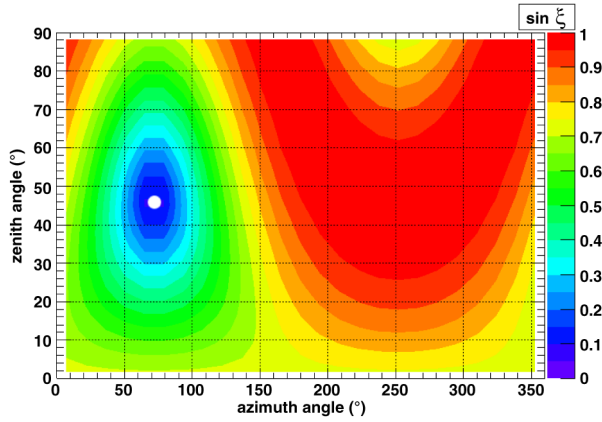
FIG. 1 (color online). Value of $\sin\xi$ versus the zenith and azimuth angles of the arrival direction of a charged particle in the ARGO-YBJ reference frame (ξ is the angle in between the magnetic field and particle direction). The white dot corresponds to particles moving parallel to $\vec{B}$.
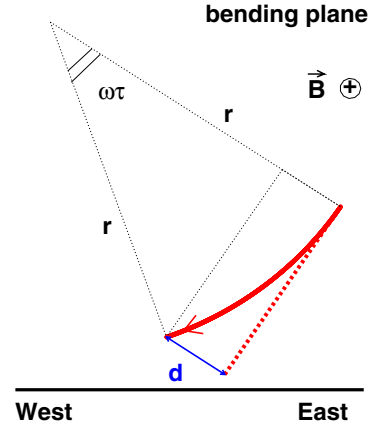

FIG. 2 (color online). The path of a secondary charged particle (bold red arrow) is modified by the GeoMF in the bending plane. The bold dotted red line is the particle path in absence of the GeoMF (the shower front is perpendicular to this line). The length d is the lateral shift on the shower front due to the magnetic effect. The black dotted lines are drawn in order to explain the formulas in Sec. III.

$$d = r[1 - \cos(\omega\tau)]. \tag{4}$$

Assuming small angular deviations ($\omega\tau \to 0$) and relativistic particles ($\beta \simeq 1$), it results

$$d = \frac{p_\perp}{2qB}(\omega\tau)^2 = \frac{qL^2}{2p}B\,\sin\,\xi. \tag{5}$$

This shift of the charged particle path in the bending plane is the main effect of the GeoMF action. As a consequence of this WE shift, there is a time-of-flight small variation ($\Delta\tau$), and taking into account the velocity component ($v_\parallel$) parallel to $\vec{B}$, a small shift ($v_\parallel\Delta\tau$) is expected also on the SN axis.

Then, Eq. (5) does not fully describe the GeoMF effect. Moreover, the model should take into account that each particle in the shower has different values of p, θ, ϕ, and L. In short, a Monte Carlo simulation is necessary in order to foresee the geomagnetic effect as a function of the shower axis direction. Anyway, Eq. (5) indicates an enlargement of the shower footprint. This implies a decrease of the particle density near the shower core, which is then balanced by an increase at larger distances, as pointed out in Ref. [3]. As a consequence. a very small, direction-dependent reduction in the ARGO-YBJ trigger efficiency can be envisaged for showers with the core lying inside the carpet. This and other features of the GeoMF effect have been simulated, and the results are presented in the next section.

the particle momentum $\vec{p}$. The value of $\sin\xi$ versus the zenith (θ) and azimuth of a particle at the YBJ site is displayed in Fig. 1. Then the magnetic effect is expected almost null in a small angular region ($\theta \sim 46°$, $\phi \sim 72°$) and maximum in a larger belt with center in $\theta \sim 44°$ and $\phi \sim 252°$.

Both the intensity and the direction of the GeoMF vary in time and depend on the altitude, but the variations are very small [18]. The variations of B, θ_B, and ϕ_B in a year are, respectively, $+40.3$ nT, $+0.1°$, $-0.01°$. From 4.3 up to 30 km above sea level, the variation of the quantity $B\sin\xi$ is less than 2%. Then the magnetic field can be assumed uniform and constant in this analysis of eight days of data.

III. SIMPLE MODEL OF THE GeoMF EFFECT

The trajectory of the EAS charged particles is deflected by the GeoMF in the plane perpendicular to $\vec{B}$ (hereafter named the bending plane). Along the direction of the GeoMF, the force is null and the velocity does not change. In the bending plane, the trajectory is circular with a radius r defined according to

$$r = \frac{p_\perp}{qB}, \tag{2}$$

where $p_\perp = p\sin\xi$ is the particle momentum in the bending plane and q its electric charge. The corresponding angular velocity is

$$\omega = \frac{qv_\perp B}{p_\perp} = \frac{qB}{\gamma m}. \tag{3}$$

The particles are shifted along the west-east (WE) axis. Neglecting another possible displacement on the south-north (SN) axis, the time of flight (τ) of the particles is simply $\tau = L/\beta c$, where L is the path length. The value (d) of the shift on the shower front (Fig. 2) is expected to be

IV. SIMULATION OF PRIMARY PROTON BEAMS

Systematic uncertainties due to assumptions adopted in a full simulation approach (primary spectrum, chemical composition, interaction model, and so on) do not allow

the study of tiny effects at the level of a few percent or less. Therefore, we preferred to simulate beams of primary protons in order to get the functional shape of the GeoMF and detector effects, whereas the huge statistics of the real data sample allows a model-independent estimate of the amplitudes of these effects.

The CORSIKA code [19] has been used to reproduce the shower development. The hadronic interactions above 80 GeV are reproduced by the SIBYLL models [20], and the low energy hadronic interactions are described by the FLUKA package [21]. A GEANT3-based code [22] is used to simulate the detector response. The primary trajectory has been projected on a $10 \times 10 \ m^2$ ground area at the center of the carpet. The simulated data are studied with the same analysis chain applied to the real data. Hereafter, the angular coordinates (θ, ϕ) define the direction of the shower axis, not that of a single particle.

A. Detector acceptance

At first, the effect of the detector acceptance was studied by simulating the showers in absence of the GeoMF. Proton beams were simulated with the same values of the primary energy (1 TeV), zenith angle (27°), interaction height (19 km), and five different values of the azimuth angle ($\phi = 0°, 45°, 90°, 135°, 180°$). The primary energy and zenith angle were chosen because they were typical values of the data sample collected by the ARGO-YBJ experiment. As a result of the simulation, the azimuthal distribution of the rate (λ) is modulated and can be fitted by the function

$$\lambda = \lambda_0 \{1 + g_{2A} \cos [2(\phi - \phi_{2A})]\}, \qquad (6)$$

where the indexes 2 and A refer to the second harmonic and the acceptance effect, respectively, and λ_0 is the mean rate. The fit parameters result in $g_{2A} = (0.2094 \pm 0.0046)\%$ and $\phi_{2A} = 88° \pm 7°$.
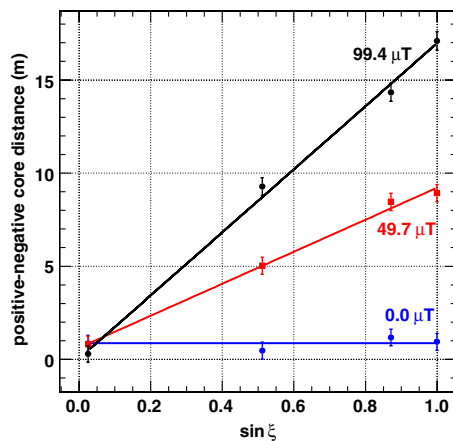
TABLE I. Angular features of the CR beams simulated to study the geomagnetic effect. The $\sin \xi$ range is fully covered.

θ (°)	ϕ (°)	$\sin \xi$
45	71.5	0.025
45	115.5	0.513
45	161.5	0.871
45	251.5	1.000

A simple geometrical simulation was performed in order to understand the origin of this azimuthal modulation with the maximum at ~90° and periodicity 180°. Modifying the detector geometry, we verified that it is due to the detector x-y asymmetry and increases with the zenith angle ($g_{2A} \propto tg^2\theta$). The modulation disappears, simulating a square detector and removing the nonactive belts along the y axis where the columns are. The modulation phase can be shifted from the expected 90° if the efficiency of the RPCs is not uniform on the entire carpet.

B. Magnetic effect

The magnetic effect was studied by means of 12 CR beams with the same values of primary energy (3 TeV), zenith angle (45°), and interaction height (19 km). The choice of the zenith angle allows coverage of the full $\sin \xi$ range. The energy has been increased with respect to the previous simulation in order to compensate the larger path in the atmosphere. Different azimuth angles (see Table I) have been used in order to get different values of the ξ angle. Three intensities of the magnetic field have been used: 0.0, 49.7 (the actual GeoMF at the YBJ site), and 99.4 μT (twice the actual GeoMF).

The shower cores have been reconstructed by using separate negative and positive particles. The results validate Eq. (5) because the distance between the positive and negative cores increases linearly with $\sin \xi$ and B (Fig. 3, left). As expected, on the basis of the simple model, when
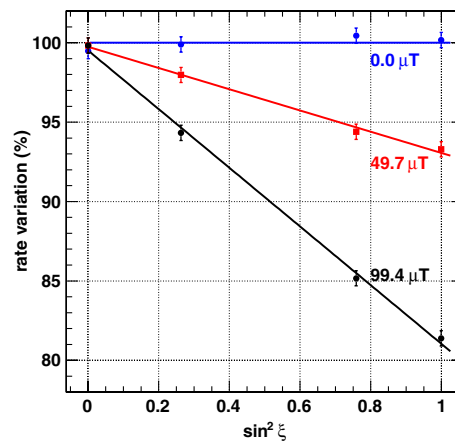

FIG. 3 (color online).   Simulation. Left: mean values of the positive-negative core distance versus $\sin \xi$ for different magnetic fields. A linear fit is superimposed. Right: fractional rate variation versus $\sin^2 \xi$ for different magnetic fields. A linear fit is superimposed.

the shower axis is nearly on the bending plane ($\theta = 45°$, $\phi = 251.5°$, $v_\parallel = 0$), the positive and negative cores are shifted truly on the WE axis with a typical shift of the order of 4.5 m for each particle.

It has been also verified that the effect of the shower stretching on the reconstruction of the EAS direction is negligible, whereas it is significant on the trigger efficiency. Neglecting the detector effect, the rate is dependent on $\sin^2 \xi$. The right plot in Fig. 3 can be fitted according to the following function:

$$\lambda = \lambda_{\max}(1 - \eta \sin^2 \xi). \tag{7}$$

It results also that the term η depends linearly on B^2. Thus, we conclude that the rate reduction is proportional to $B^2 \sin^2 \xi$. Therefore, the rate decrease is related to the GeoMF stretching of the EAS footprint. In other words, the decrease of the charge density close to the core actually reduces the trigger efficiency when the core is on the array.

To explain this result, we must take into account that the enlargement of the lateral distribution has two contrary effects: the more separated particles can fire more pads; on the contrary, the enlargement can reduce the number of hits on the central carpet (trigger area). Looking at the simulated events, we verify that the second one is the leading effect; therefore, the trigger reduction is essentially a boundary effect.

Before closing the section, we want remind that the CR-beam simulations do not allow a full estimate of the GeoMF and detector effects but indicate only their functional shape. The amplitudes of these effects are precisely determined by the analysis of the real data sample.

V. WHAT TO EXPECT

Combining Eqs. (6) and (7), the number of showers (N_θ) with cores on carpet in an angular window $\Delta\theta \times \Delta\phi$ around a fixed zenith angle is

$$N_\theta = N_{\theta,\max}(1 - \eta\sin^2 \xi)\{1 + g_{2A} \cos[2(\phi - \phi_{2A})]\}, \tag{8}$$

where $N_{\theta,\max}$ is the number of events expected without a magnetic field (the average value with respect to ϕ).

At the beginning, we can neglect the detector factor in order to point out the GeoMF effect. Equation (8) becomes

$$N_\theta = N_{\theta,\max}(1 - \eta\sin^2 \xi), \tag{9}$$

where the angle ξ can be calculated by using the direction cosines of the shower (l, m, and n) and those of the GeoMF (l_B, m_B, and n_B). The formalism can be simplified by introducing another azimuth angle Φ defined as $\Phi = \phi - \phi_B$. According to this definition, $\Phi_B = 0$; therefore, the angle ξ is given by the equation

$$\cos \xi = ll_B + mm_B + nn_B =$$
$$= \sin\theta \sin\theta_B \cos\Phi + \cos\theta \cos\theta_B.$$

Then, it is straightforward to calculate

$$\sin \xi = \sqrt{A_0 + A_1 \cos\Phi + A_2 \cos(2\Phi)}, \tag{10}$$

where

$$A_0 = \sin^2\theta_B + \left(1 - \frac{3}{2}\sin^2\theta_B\right)\sin^2\theta,$$

$$A_1 = -\frac{1}{2}\sin 2\theta_B \sin 2\theta,$$

$$A_2 = -\frac{1}{2}\sin^2\theta_B\sin^2\theta. \tag{11}$$

The first term is positive, whereas A_1 and A_2 are negative. A two-harmonics function is obtained combining Eqs. (9) and (10) and referring back to the previous azimuth angle

$$N_\theta = N_{\theta,0}\{1 + g_1 \cos(\phi - \phi_1) + g_2 \cos[2(\phi - \phi_2)]\}, \tag{12}$$

where

$$\phi_1 = \phi_2 = \phi_B, \tag{13}$$

$$N_{\theta,0} = N_{\theta,\max}(1 - \eta A_0), \tag{14}$$

$$g_1 = -\frac{\eta A_1}{1 - \eta A_0} = \frac{\eta \sin 2\theta_B}{2(1 - \eta A_0)}\sin 2\theta, \tag{15}$$

$$g_2 = -\frac{\eta A_2}{1 - \eta A_0} = \frac{\eta\sin^2\theta_B}{2(1 - \eta A_0)}\sin^2\theta. \tag{16}$$

$N_{\theta,0}$ in Eq. (14) represents the ϕ average at fixed θ of the number of events in ϕ bins reduced by the effect of shower stretching on the trigger, and ηA_0 is the reduction percentage.

Taking into account also the detector factor according to Eq. (8) and assuming $g_1 g_{2A} \simeq 0$, $g_2 g_{2A} \simeq 0$, Eq. (12) becomes

$$N_\theta = N_{\theta,0}\{1 + g_1 \cos(\phi - \phi_1) + g_2 \cos[2(\phi - \phi_2)]$$
$$+ g_{2A} \cos[2(\phi - \phi_{2A})]\}, \tag{17}$$

where the first harmonic is exclusively due to the GeoMF, and the second harmonic is split in two terms: one with amplitude g_2 and phase ϕ_2 is due to the GeoMF; the other one with amplitude g_{2A} and phase ϕ_{2A} is due to the detector acceptance.

VI. ANALYSIS OF INTERNAL-CORE SHOWERS

A. Data sample

The data set was collected during the period October 7–14, 2010 (6.77×10^5 s). The RPC efficiency was monitored by means of a five-layer telescope [23], and in that period it was $\sim 96.7\%$.

Two analysis cuts were applied in order to select internal-core events: the shower core must be reconstructed inside a square of 40×40 m^2 at the center of the carpet, and the zenith angle must be lower than 60°. The first cut was chosen in order to make more evident the trigger efficiency decrease (the effect is expected very different for showers with cores far from the detector). The second one simplifies the analysis because in that zenith angle range, the detector effect does not prevail on the magnetic one. These cuts guarantee also a more reliable reconstruction of the shower direction. After these cuts, more than 347×10^6 events survive with a mean rate of 512.8 Hz. A very short analysis has been performed also for external-core showers (Sec. VII).

B. Timing calibration

Small errors in the reconstruction of the shower direction may introduce large systematic errors in the azimuthal distribution, especially for small zenith angles. Thus, the 18,360 pads were carefully time calibrated by means of a software procedure based on the characteristic plane method [24].

C. Rate versus $\sin^2 \xi$

The dependence of the number of events on $\sin^2 \xi$ is well represented in Fig. 4, where the number of events in an angular window $\Delta\theta \times \Delta\phi = 2° \times 5°$ is plotted versus $\sin^2 \xi$. The θ value is fixed for each aligned group of points while ϕ is running. The $\sin^2 \xi$ range depends on θ (see Fig. 1) being maximum for $\theta = 45°$ and minimum for θ close to 0°. The scattered points can be fitted by means of function (9), which is then confirmed to give a good description of the data. This fit does not separate GeoMF and detector effects, and we have analytically verified that η would be overestimated. Therefore, a fit has been implemented by using function (8) with four parameters ($N_{\theta,\max}$, η, g_{2A}, and ϕ_{2A}). For the lower values of the zenith angle, the fit is not reliable because the detector effect is too small. Then we used a two-step fit: from the fit for the zenith angles higher than 12°, we estimate the phase $\phi_{2A} = 96.5° \pm 3.4°$ (Fig. 5). The fit errors are large, but the parameter value is very stable. Then we fix ϕ_{2A} in function (8) and perform the fit in the whole θ range. The fit results for η and g_{2A} are shown in Fig. 6; the first point ($\theta \sim 1°$) is not displayed because the $\sin^2 \xi$ range is too small, the uncertainty on ϕ is very high, and then the fit is not reliable for this zenith value.

As a result of this fit, we conclude that $\eta = (4.093 \pm 0.068)\%$ does not show any dependence on the zenith
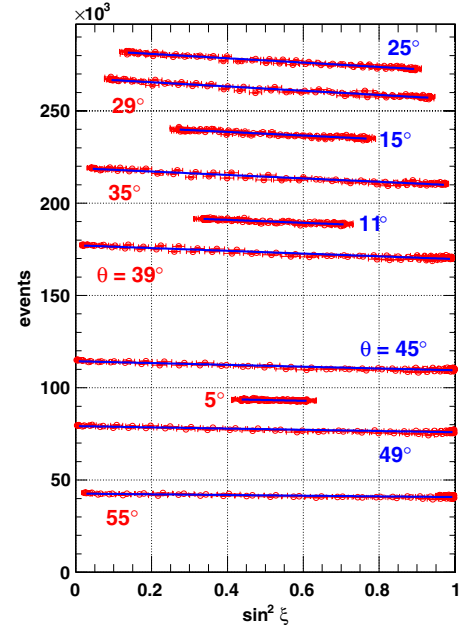

FIG. 4 (color online). Real data: scatter plot of the number of events in angular windows $\Delta\theta \times \Delta\phi = 2° \times 5°$ versus $\sin^2 \xi$ for different values of θ. Fits with function (9) are superimposed.

angle, and the detector coefficient g_{2A} has the expected dependence on the zenith angle ($g_{2A} = \epsilon tg^2\theta$).

By using Eq. (8) in order to confirm the validity of this procedure, we have defined a corrected number of events

$$N_\theta^* \equiv N_\theta / \{1 + g_{2A} \cos[2(\phi - \phi_{2A})]\}$$
$$= N_{\theta,\max}(1 - \eta \sin^2 \xi), \quad (18)$$

where the detector parameters (g_{2A}, ϕ_{2A}) of the previous fit have been used to calculate N_θ^*. As an example, the scatter plots of N_θ and N_θ^* versus $\sin^2 \xi$ are shown in Fig. 7 for
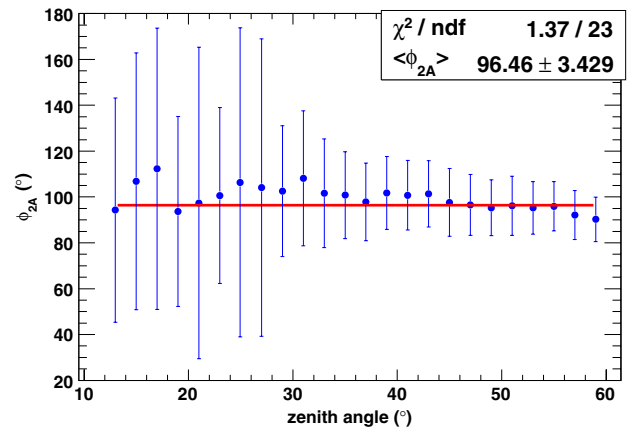

FIG. 5 (color online). Real data: the phase (ϕ_{2A}) of the detector effect versus the zenith angle. The values of ϕ_{2A} are estimated by means of a fit of N_θ versus $\sin^2 \xi$ and ϕ using function (8). Below 30° in the zenith, the phase shows large errors due to the vanishing small size of the coefficient g_{2A} (see Fig. 6, right).
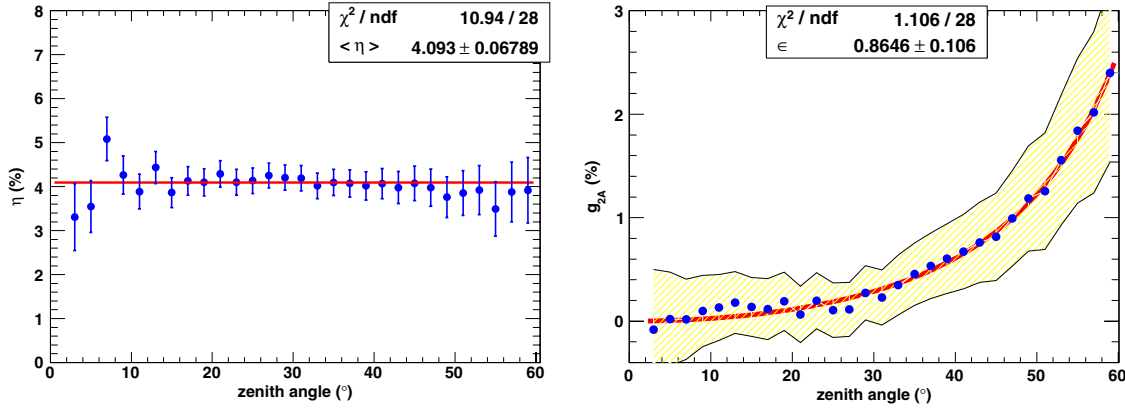
FIG. 6 (color online).   Real data: the coefficients η (left) and g_{2A} (right) versus θ. The values of η and g_{2A} are estimated by fitting N_θ versus $\sin^2 \xi$ and ϕ according to function (8). In the right plot, the colored area represents 1σ uncertainty, and the fit according to $g_{2A} = \epsilon tg^2\theta$ is superimposed.

$\theta = 35°$. The fit with functions (9) and (18) works better for N_θ^* ($\chi^2/ndf = 1.2$) than for N_θ ($\chi^2/ndf = 3.2$). This result confirms that the detector effect has been properly estimated. Similar improvements are observed for the other θ values.

D. Azimuthal distribution

The azimuthal distribution obtained by integrating all the showers in the range $\theta < 60°$ can be fitted by the double harmonic function (12). The fit result is shown in Fig. 8; the phase of the first harmonic ($\phi_1 = 72.75° \pm 0.29°$) is compatible within 3σ with the GeoMF azimuth ($\phi_B = 71.89°$), as expected if the origin of the modulation is geomagnetic. This is not the case of the second-harmonic phase ($\phi_2 = 87.00° \pm 0.40°$) with a value in between those expected for the detector and GeoMF effects.

The high value of χ^2/ndf is mainly due to some inefficiencies at $\phi \sim n\ 90°$ ($n = 0, 1, 2, 3$). The origin of these dips is not fully clear. Their position in the azimuthal distribution indicates a relation with the detector shape and the framework of the experimental hall. We suppose they could be shadows of iron beams and columns. Anyway, the presence of these dips does not invalidate this analysis on the GeoMF effect. To take into account the dips, we assume that they have a Gaussian shape (with angular width σ and amplitude k). Then the fit is performed with the following function:

$$N = N_0\{1 + g_1 \cos(\phi - \phi_1) + g_2 \cos[2(\phi - \phi_2)]$$
$$+ k(e^{-\phi^2/2\sigma^2} + e^{-(\phi-90)^2/2\sigma^2} + e^{-(\phi-180)^2/2\sigma^2}$$
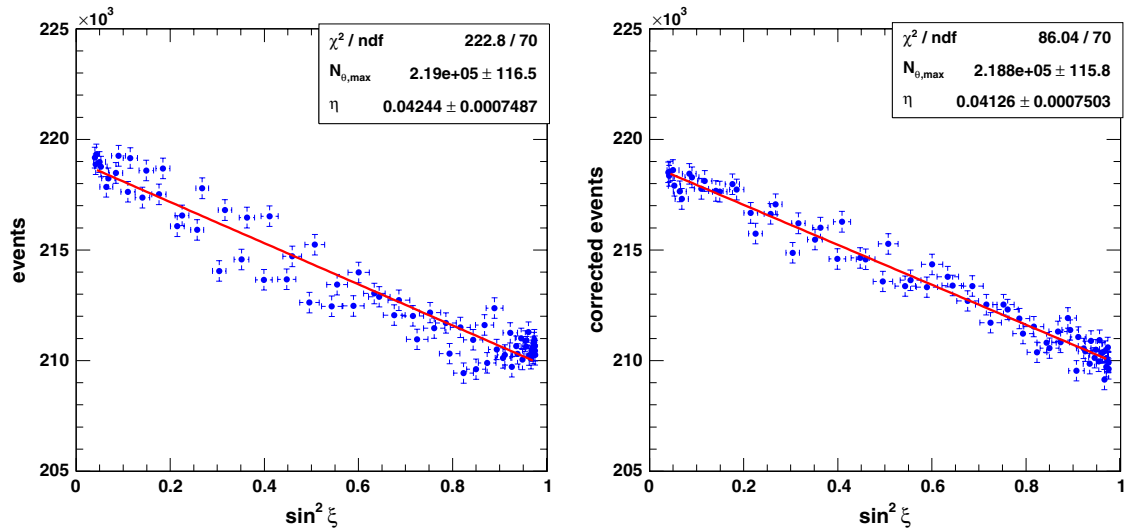$$+ e^{-(\phi-270)^2/2\sigma^2} + e^{-(\phi-360)^2/2\sigma^2})\}. \quad (19)$$

FIG. 7 (color online).   Real data in angular windows $\Delta\theta \times \Delta\phi = 2° \times 5°$ centered at $\theta = 35°$. Left: scatter plot of the number of events (N_θ) versus $\sin^2 \xi$ fitted with function (9). Right: scatter plot of the corrected number of events (N_θ^*) versus $\sin^2 \xi$, the correction and fit are performed according to function (18). A sharp reduction of the χ^2/ndf value is visible when the corrected number of events is used.
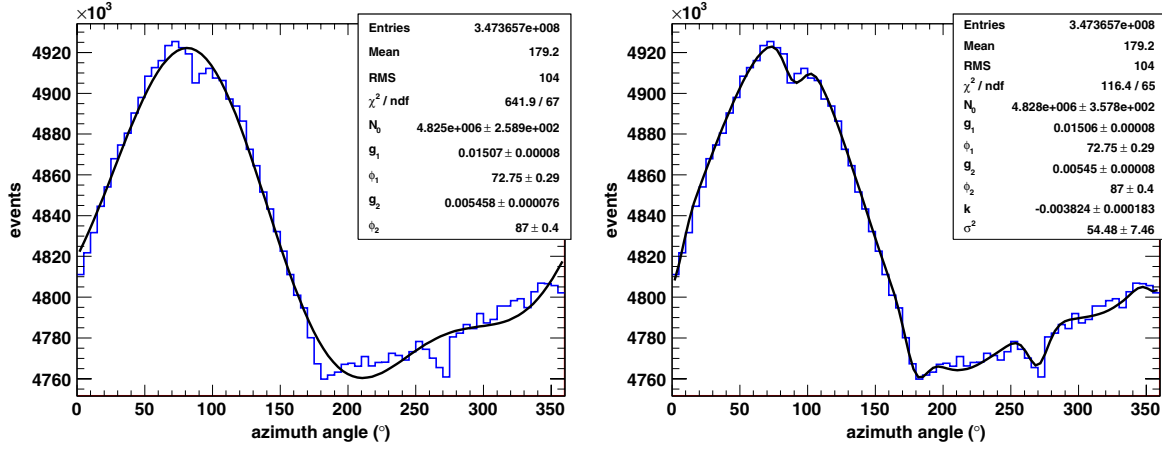
FIG. 8 (color online). Real data: the azimuthal distribution fitted with function (12) (left) and function (19) (right).

The result of the new fit is shown in the right panel of Fig. 8. The χ^2/ndf becomes smaller ($116/65 = 1.8$) with respect to that ($642/67 = 9.6$) of the fit in the left panel of Fig. 8. The parameters g_1, ϕ_1, g_2, and ϕ_2 do not change in this second fit. The dip amplitude is $k = -(0.382 \pm 0.018)\%$, and the Gaussian width is $\sigma = 7.38° \pm 0.51°$.

E. Amplitudes g_1 and g_2 as functions of θ

The azimuthal distribution has been studied also in θ ranges of $2°$ in order to check the dependence of g_1 and g_2 on θ. Also, in this case, function (12) has been used. The result for g_1 is shown in Fig. 9. By fitting the experimental points with function (15), we can confirm that η does not depend on θ, and its estimate is very close to the previous one (Fig. 6, left). The fractional variation of the term $(1 - \eta A_0)$ is less than 0.7%. Then, g_1 is mainly proportional to $\sin 2\theta$.

According to Eq. (16), g_2 is expected to be mainly proportional to $\sin^2 \theta$; however, the data do not match with the expected shape, and the value of η from the fit is in
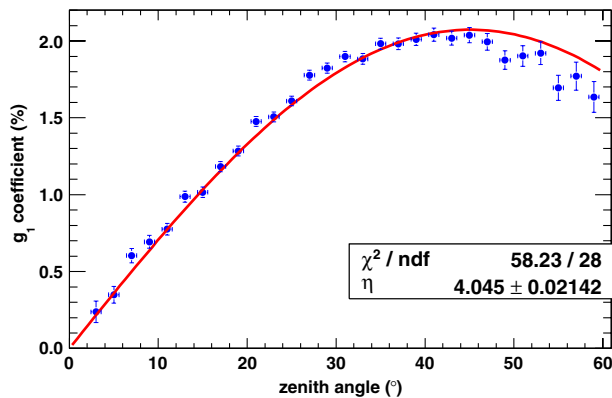

FIG. 9 (color online). Real data: the coefficient g_1 versus the zenith angle. The fit with function (15) has been applied.

disagreement with the previous estimates. This result is not odd because we know that the GeoMF and detector effects are not disentangled in the second harmonic of function (12).

F. Two components in the second harmonic

While the first harmonic is in full agreement with the GeoMF model, this is not the case for the second harmonic. The tension can be solved by simply taking into account that the detector effect operates on the second harmonic and that the proper function to fit the azimuthal distribution is function (17). Thus, three different data sets were selected on the basis of the zenith angle in order to disentangle the two second-harmonic components. The ϕ distributions of the subsamples (named α for $\theta < 20°$, β for $20° < \theta < 40°$, and γ for $40° < \theta < 60°$) are shown in Fig. 10 and can be fitted all together with a single function:

$$N_i = N_{i,0}\left\{1 + \frac{\eta \sin 2\theta_B}{2(1-\eta A_0)}\langle\sin 2\theta\rangle_i \cos(\phi - \phi_1)\right.$$

$$+ \frac{\eta \sin^2\theta_B}{2(1-\eta A_0)}\langle\sin^2\theta\rangle_i \cos[2(\phi - \phi_1)]$$

$$\left. + g_{2A}^i \cos[2(\phi - \phi_{2A})]\right\}, \tag{20}$$

where the coefficients of the magnetic components (g_1 and g_2) are deduced from Eqs. (15) and (16), the phase ϕ_1 is used for the first and second magnetic harmonics, and the index $i = \alpha, \beta, \gamma$ indicates the subsamples. Then, the fit parameters are $N_{\alpha,0}$, $N_{\beta,0}$, $N_{\gamma,0}$, η, ϕ_1, g_{2A}^α, g_{2A}^β, g_{2A}^γ, and ϕ_{2A}. The new fit works very well (the results are shown in Table II); however, the χ^2/ndf value is higher ($1053/207 = 5.1$) when the dip correction is not applied. It reduces to $481/201 = 2.4$ by adding the negative Gaussians for the dips. The phase ϕ_1 and the GeoMF azimuth ϕ_B are in agreement;
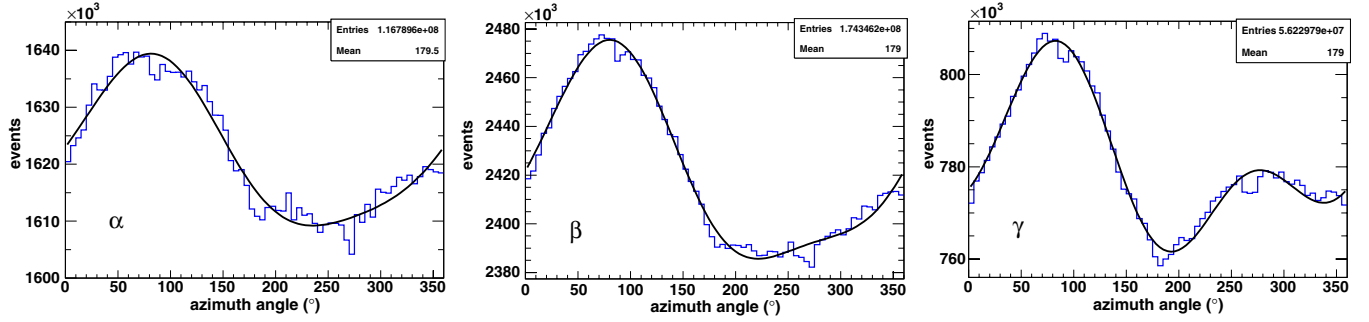
FIG. 10 (color online).   Real data: the azimuthal distribution in different θ ranges (0°–20°, 20°–40°, and 40°–60°). The fit with function (20) is superimposed (see Table II for the fit parameters).

the η value is fully compatible with the previous estimates. The coefficients g_{2A}^i increase with θ and $\phi_{2A} \simeq 96°$ according to the results of the previous fit (Figs. 5 and 6, right).

G. Final remarks

The azimuthal distribution depends on a mix of magnetic and detector effects, whose contributions are shown in Fig. 11 where the coefficients g_1, g_2, and g_{2A} are plotted as functions of the zenith angle according to formulas (15) and (16), Fig. 6, right, and Table II. This plot suggests that the GeoMF origin of the rate reduction is leading with respect to the detector effect in the zenith range 20°–40°, where $g_{2A} \ll g_1$. For $\theta > 45°$, the increase of g_2 and g_{2A} and the decrease of g_1 suggest that the second harmonic is dominant in the azimuthal distribution at high zenith angles. We verified this in the data by fitting the azimuthal distribution in the range $60° < \theta < 80°$. The amplitude of the second-harmonic is almost 4 times greater than the amplitude of the first one.

The measurement of η has been repeated with three different methods obtaining compatible results. We conclude that $\eta = (4.055 \pm 0.014)\%$ is the proper estimate for this analysis of the ARGO-YBJ data. Different values are expected applying other cuts on the core position (see the next section). The coefficient η depends also on the geomagnetic latitude and altitude of the site, detector features, and trigger requirements.

TABLE II.   Results of the fit with function (20) of the distributions in Fig. 10.

η (%)	4.060 ± 0.019
ϕ_1 (°)	72.22 ± 0.28
g_{2A}^α (%)	0.124 ± 0.013
g_{2A}^β (%)	0.271 ± 0.011
g_{2A}^γ (%)	1.076 ± 0.019
ϕ_{2A} (°)	96.30 ± 0.47

VII. EXTERNAL-CORE SHOWERS

An increase of the charge density is expected far from the EAS core, as a counterbalance to the decrease close to the cores (see, also, Ref. [3]). Then, a GeoMF increase of the trigger efficiency is expected for showers with core outside the ARGO-YBJ carpet. In analogy with Eq. (9), the number of external events (N_θ^{out}) in an angular window $\Delta\theta \times \Delta\phi$ around a fixed zenith angle may depend on ξ as

$$N_\theta^{out} = N_{\theta,min}^{out}(1 + \eta_{out}\sin^2\xi), \qquad (21)$$

where $N_{\theta,min}^{out}$ is the number of events expected without a magnetic field, and η_{out} is the parameter analogous to η (with opposite sign).

A sample of external showers was selected requiring a core reconstructed outside a 120 m square centered on the ARGO-YBJ carpet. A short analysis confirms the validity of Eq. (21). Indeed, Fig. 12 is very similar to Fig. 4 with opposite slopes. The value of η_{out} is ~2.5%.

VIII. ABSOLUTE POINTING ACCURACY OF AN EAS ARRAY

The Moon shadow analysis [25] is commonly used to check the absolute pointing of EAS arrays. It requires
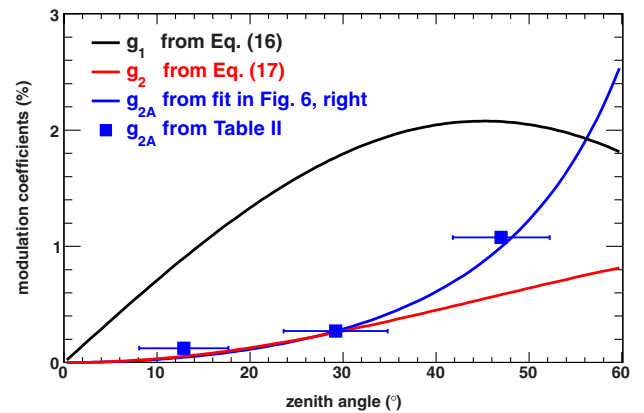

FIG. 11 (color online).   Real data: the coefficients g_1, g_2, and g_{2A} versus θ from formulas (15) and (16), Table II, and the fit in Fig. 6, right. The experimental points are drawn at the mean θ value and the error bars are the RMS of the θ distribution.
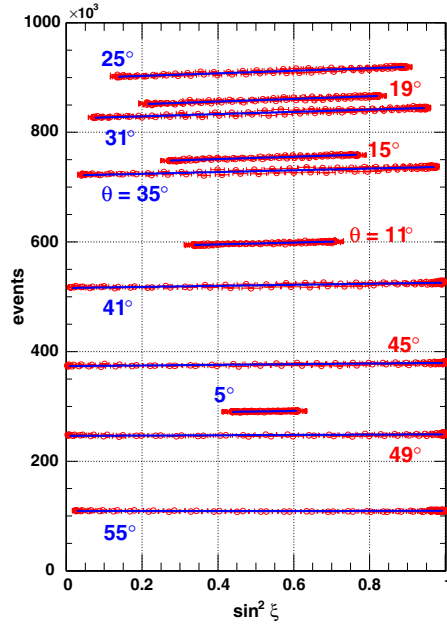
FIG. 12 (color online).   Showers with cores outside the detector area: scatter plot of the number of events in angular windows $\Delta\theta \times \Delta\phi = 2° \times 5°$ versus $\sin^2 \xi$ for different values of θ. Fits with function (21) are superimposed.

very large samples of showers, and the pointing accuracy cannot be checked daily. The GeoMF effect on EAS suggests another method to control the array pointing accuracy. Indeed, only the first harmonic of the azimuthal distribution contributes to the mean values of the direction cosines ($\langle l \rangle$, $\langle m \rangle$), and a fast check of the ϕ_1 value is possible also using small samples of internal-core events:

$$\phi_1 = \arctan \frac{\langle m \rangle}{\langle l \rangle}. \qquad (22)$$

When $\phi_1 \neq \phi_B$, a systematic correction is necessary. The direction cosines must be increased or reduced in order to get the expected mean values

$$\langle l \rangle = \frac{\eta \sin 2\theta_B}{4} \cos \phi_B \left\langle \frac{\sin 2\theta \sin \theta}{1 - \eta A_0} \right\rangle,$$

$$\langle m \rangle = \frac{\eta \sin 2\theta_B}{4} \sin \phi_B \left\langle \frac{\sin 2\theta \sin \theta}{1 - \eta A_0} \right\rangle. \qquad (23)$$

The only requirement to perform the pointing correction is to estimate precisely the reduction factor η for the data sample used in the analysis.

IX. CONCLUSIONS

The effect of the geomagnetic Lorentz force on EAS charged particles has been studied in a data sample collected by the ARGO-YBJ experiment. The shower extension enlarges depending on the arrival direction with respect to the GeoMF and the modified density of charged particles slightly reduces the trigger efficiency for EAS with cores on the detector. The GeoMF effect and the trigger efficiency decrease are understood by means of a model complemented by Monte Carlo simulations and verified in a large real data sample.

The nonuniform azimuthal distribution was deeply studied. It is well described by two harmonics: the first one of about 1.5% and the second one of about 0.5%. The first harmonic is due to the GeoMF; the second one is the sum of the magnetic and detector effects. The measurement of the geomagnetic phase ($\phi_1 = 72.22° \pm 0.28°$) is fully compatible with the expected value ($\phi_B = 71.89°$). Other checks confirm the geomagnetic origin of the modulation. A GeoMF effect with opposite sign has been observed also for showers with cores outside the detector area.

The phase of the first harmonic (ϕ_1) can be used as a marker of the absolute pointing of EAS arrays. When necessary, a simple correction of the absolute pointing can be applied.

To our knowledge, the experimental results presented here are the first evidence of the charge density reduction near the EAS axis due to the GeoMF.

ACKNOWLEDGMENTS

[1] T. H. Johnson, Phys. Rev. **43**, 834 (1933); L. W. Alvarez and A. H. Compton, Phys. Rev. **43**, 835 (1933); T. H. Johnson and E. C. Stevenson, Phys. Rev. **44**, 125 (1933).

[2] G. Cocconi, Phys. Rev. **93**, 646 (1954); **95**, 1705(E) (1954).

[3] A. A. Ivanov, V. P. Egorova, V. A. Kolosov, A. D. Krasil'nikov, M. I. Pravdin, and I. E. Sleptsov, JETP Lett. **69**, 288 (1999).

[4] M. Bahmanabadi, A. Anvari, M. Khakian Ghomi, D. Purmohammad, J. Samimi, and M. L. Rachti, Exp. Astron. **13**, 39 (2002); M. Khakian Ghomi, M. Bahmanabadi, J. Samimi, A. Anvari, and F. Sheidaei, in *Proceedings of the 30th International Cosmic Ray Conference, Merida, 2007* edited by R. Caballero, J. C. D'Olivo, G. Medina-Tanco, L. Nellen, F. A. Sánchez, and J. F. Valdés-Galicia, (Universidad Nacional Autónoma de México, Mexico, 2008) Vol. **4**, p. 11.

[5] D. Ardouin *et al.* (CODALEMA Collaboration), Astropart. Phys. **31**, 192 (2009).

[6] A. Cillis and S. J. Sciutto, J. Phys. G **26**, 309 (2000).

[7] S. C. Commichau, A. Biland, J. L. Contreras, R. de los Reyes, A. Moralejo, J. Sitarek, and D. Sobczyńska, Nucl. Instrum. Methods Phys. Res., Sect. A **595**, 572 (2008).

[8] J. N. Capdevielle, C. Le Gall, Kh. N. Sanosyan, Astropart. Phys. **13**, 259 (2000).

[9] P. Abreu *et al.* (Pierre Auger Collaboration), J. Cosmol. Astropart. Phys. 11 (2011) 022.

[10] H. H. He *et al.*, in *Proceedings of the 29th International Cosmic Ray Conference, Pune, 2005* Vol. **6**, pp. 5–8.

[11] P. Bernardini *et al.*, arXiv:1110.0670; P. Bernardini and S. N. Sbano, J. Phys. Conf. Ser. **409**, 012229 (2013); S. N. Sbano, Nucl. Phys. B, Proc. Suppl. **239–240**, 274 (2013).

[12] G. Aielli *et al.* (ARGO-YBJ Collaboration), Nucl. Instrum. Methods Phys. Res., Sect. A **661**, S50 (2012).

[13] G. Aielli *et al.* (ARGO-YBJ Collaboration), Astrophys. J. Lett. **714**, L208 (2010); B. Bartoli *et al.* (ARGO-YBJ Collaboration), Astrophys. J. **734**, 110 (2011); B. Bartoli *et al.* (ARGO-YBJ Collaboration), Astrophys. J. Lett. **745**, L22 (2012); B. Bartoli *et al.* (ARGO-YBJ Collaboration), Astrophys. J. **758**, 2 (2012); B. Bartoli *et al.* (ARGO-YBJ Collaboration), Astrophys. J. **760**, 110 (2012); B. Bartoli *et al.* (ARGO-YBJ Collaboration), Astrophys. J. **767**, 99 (2013); B. Bartoli *et al.* (ARGO-YBJ Collaboration), Astrophys. J. **779**, 27 (2013).

[14] G. Aielli *et al.* (ARGO-YBJ Collaboration), Phys. Rev. D **80**, 092004 (2009); G. Aielli *et al.* (ARGO-YBJ Collaboration), Astrophys. J. **729**, 113 (2011); B. Bartoli *et al.* (ARGO-YBJ Collaboration), Phys. Rev. D **85**, 022002 (2012); B. Bartoli *et al.* (ARGO-YBJ Collaboration), Phys. Rev. D **85**, 092005 (2012); B. Bartoli *et al.* (ARGO-YBJ Collaboration), Phys. Rev. D **88**, 082001 (2013).

[15] G. Aielli *et al.* (ARGO-YBJ Collaboration), Nucl. Instrum. Methods Phys. Res., Sect. A **562**, 92 (2006).

[16] M. Iacovacci *et al.* (ARGO-YBJ Collaboration), in *Proceedings of the 33rd International Cosmic Ray Conference, Rio de Janeiro, 2013* (Report No. CR-IN 1035).

[17] G. Aielli *et al.* (ARGO-YBJ Collaboration), Astropart. Phys. **30**, 85 (2008); G. Aielli *et al.* (ARGO-YBJ Collaboration), Astrophys. J. **699**, 1281 (2009).

[18] www.ngdc.noaa.gov.

[19] D. Heck *et al.*, Report No. FZKA 6019, 1998 [see, also, http://www-ik.fzk.de/~corsika/physics_description/corsika_phys.html].

[20] R. Engel, T. K. Gaisser, T. Stanev, and P. Lipari, in *Proceedings of the 26th International Cosmic Ray Conference, Salt Lake City, 1999* edited by D. B. Kieda, M. B. Salamon, and B. L. Dingus, (AIP Conference Proceedings, New York, 1999) Vol. **1**, p. 415; E. J. Ahn, R. Engel, T. K. Gaisser, P. Lipari, and T. Stanev, Phys. Rev. D **80**, 094003 (2009).

[21] A. Fassò, P. R. Sala, A. Fasso, J. Ranft, Reports No. CERN-2005-10, 2005, No. INFN/TC_05/11, and No. SLAC-R-773, www.slac.stanford.edu/cgi-wrap/getdoc/slac-r-773.pdf; G. Battistoni, F. Cerutti, A. Fassò, A. Ferrari, S. Muraro, J. Ranft, S. Roesler, and P. R. Sala, AIP Conf. Proc. **896**, 31 (2007); G. Battistoni, A. Margiotta, S. Muraro, and M. Sioli, Nucl. Instrum. Methods Phys. Res., Sect. A **626–627**, S191 (2011) [see, also, www.fluka.org].

[22] CERN Report No. W5013, 1993.

[23] G. Aielli *et al.* (ARGO-YBJ Collaboration), Nucl. Instrum. Methods Phys. Res., Sect. A **608**, 246 (2009).

[24] H. H. He, P. Bernardini, A. K. Calabrese Melcarne, and S. Z. Chen, Astropart. Phys. **27**, 528 (2007); G. Aielli *et al.* (ARGO-YBJ Collaboration), Astropart. Phys. **30**, 287 (2009).

[25] B. Bartoli *et al.* (ARGO-YBJ Collaboration), Phys. Rev. D **84**, 022003 (2011).